Research Article Vol. 10, No. 6 / June 2023 / Optica 801

Ultra-CEP-stable single-cycle pulses at 2.2 μm

Maciej Kowalczyk,[1,2,3,†] Nathalie Nagl,[1,3,5,†] Philipp Steinleitner,[3,6,†] Nicholas Karpowicz,[3] Vladimir Pervak,[1] Aleksander Głuszek,[4] Arkadiusz Hudzikowski,[4] Ferenc Krausz,[1,2,3] Ka Fai Mak,[3] and Alexander Weigel[2,3,*]

[1]Fakultät für Physik, Ludwig-Maximilians-Universität München, Am Coulombwall 1, 85748 Garching, Germany
[2]Center for Molecular Fingerprinting Research (CMF), 1093 Budapest, Czuczor Utca 2-10, Hungary
[3]Max-Planck-Institut für Quantenoptik, Hans-Kopfermann-Str. 1, 85748 Garching, Germany
[4]Laser & Fiber Electronics Group, Faculty of Electronics, Photonics and Microsystems, Wrocław University of Science and Technology, Wybrzeże Wyspiańskiego 27, 50-370 Wrocław, Poland
[5]nathalie.nagl@mpq.mpg.de
[6]philipp.steinleitner@mpq.mpg.de
[†]These authors contributed equally to this work.
*alexander.weigel@mpq.mpg.de

Received 21 December 2022; revised 28 April 2023; accepted 11 May 2023; published 21 June 2023

Single-cycle optical pulses with controllable carrier-envelope phase (CEP) form the basis to manipulate the nonlinear polarization of matter on a sub-femtosecond time scale. Moreover, nonlinear light–matter energy exchange and frequency conversion processes benefit from longer, infrared wavelengths. We report a highly stable source of 6.9-fs, single-cycle pulses at 2.2 μm, based on a directly diode-pumped Cr:ZnS oscillator with 22.9-MHz repetition rate. Extreme spectral broadening of the oscillator output to a super-octave bandwidth (1.1–3.1 μm) is achieved in a single rutile (TiO_2) plate. Excellent agreement with simulations provides a precise understanding of the underlying nonlinear pulse propagation. A comprehensive investigation of alternative broadening materials and additional simulations single out the exceptional broadening in TiO_2 due to the favorable interplay of self-focusing, and plasma formation accompanied by self-phase modulation and self-compression. Unprecedented reproducibility of the single-cycle waveforms is ensured by a unique combination of active CEP stabilization with a residual CEP jitter of only 5.9 mrad (0.1 Hz to 11.45 MHz) and a relative intensity noise of 0.036% (0.1 Hz to 1 MHz). The new single-cycle source permits efficient downconversion to the mid-infrared by cascaded intra-pulse difference frequency generation, giving access to sub-femtosecond manipulation of electric currents in low-bandgap materials with an unprecedented degree of control.

https://doi.org/10.1364/OPTICA.481673

1. INTRODUCTION

The temporal confinement of laser pulses to a single field oscillation cycle has opened a new research area by allowing generation of isolated attosecond pulses [1] and studying electronic motion in atoms and molecules in real time [2–4]. Waveform-controlled single-cycle pulses have not only provided new insights into fundamental physical phenomena, but also enabled the control of atomic-scale electron dynamics on their genuine sub-femtosecond time scales [5–7]. This technology can be harnessed for a new generation of light-wave-driven electronics, in which electric currents are manipulated at previously unattainable terahertz to petahertz rates [8]. It also provides new diagnostic tools for complete electric-field characterization of ultrashort laser pulses [9–11].

When implemented in the gas-phase, strong-field phenomena (such as high-harmonic generation, HHG) require high-power microjoule- or millijoule-level laser pulses available only at reduced repetition rates, with subsequent spectral broadening in thin bulk plates [12], gas cells [13], or hollow-core fibers [14–16]. By contrast, in condensed matter, strong-field processes, such as, e.g., the tunneling through nanoscopic gaps [17], can be already induced at moderate, sub-nanojoule-level pulse energies, directly available from multi-megahertz-rate laser oscillators [18,19].

Kerr-lens mode-locked (KLM) Ti:sapphire lasers have been the gold standard for providing waveform-controllable pulses at megahertz rates for more than two decades [20]. Meanwhile, they routinely generate pulses with octave-spanning spectra and durations approaching a single optical cycle [21,22]. Despite their wide proliferation and 30 years of maturation, the range of applications of KLM Ti:sapphire lasers has been constrained by their near-infrared emission spectrum. For instance, processes such as light-wave-driven carrier dynamics in low-bandgap semiconductors are not directly accessible and require complex and inefficient additional frequency downconversion [23,24]. Fueled by this shortcoming, extensive efforts have been made to develop laser sources of few-cycle light at longer, infrared wavelengths. Single-cycle pulses spectrally centered at 1.5 μm and 2 μm have been recently demonstrated, based on amplified fiber lasers with

erbium [25,26] and erbium/thulium dopings [27], combined with spectral broadening and compression in highly nonlinear fibers.

Bulk lasers based on chromium (Cr^{2+})-doped II-VI semiconductors have emerged as promising alternatives to fiber-based approaches for infrared pulse generation [28–34]. Due to their broadband emission in the range between 2 and 3 μm, Cr:ZnS/ZnSe gain media have also been termed the "Ti:sapphire of the mid-IR" [28]. Their long-wavelength emission is ideal for direct frequency-comb spectroscopy [35], efficient frequency downconversion to the mid-IR [36,37], and extending the cutoff frequency of HHG [38]. Moreover, direct diode pumping of an oscillator [33,37,39], and a post-amplifier [40] resulted in ultralow amplitude noise at megahertz repetition rates—a key requisite for performing electric-field-driven applications at the highest precision and sensitivity. Pulse durations directly achievable from Cr^{2+}-doped II-VI oscillators are limited to the few-cycle regime [41,42]. Approaching the single-cycle regime calls for external spectral broadening and dispersive temporal compression. Spectral broadening in ZnS/ZnSe [42,43] and step-index fluoride fibers [44] has been demonstrated but could not reach pulse durations of less than two optical cycles. Only recently, spectral broadening in a bulk rutile (TiO_2) plate combined with tailored dispersive optics has allowed compression of pulses generated directly by a Cr:ZnS oscillator down to a single optical cycle [37]. Yet, the physical mechanisms underlying the remarkable performance of this simple, robust, and highly efficient bulk compression scheme have remained to be explored.

The generation of reproducible and controllable single-cycle waveforms requires pulse-to-pulse stabilization of their carrier-envelope phase (CEP). Passive CEP stabilization via frequency-mixing and downconversion [45] comes at the expense of low single-pass conversion efficiency and change in center wavelength, so that additional conversion and amplification is needed [26,46]. Active CEP stabilization provides waveform-stable output pulses directly from the oscillator by detecting the carrier-envelope-offset frequency (f_{ceo}) interferometrically [47] and maintaining it at zero value, using electronic feedback [20] or feed-forward loops [48]. The latter has allowed reaching the highest f_{ceo} stability so far with a residual integrated phase noise down to 3.5 mrad (in the range between 1 Hz and 3 MHz) for a laser producing multi-cycle, 60-fs pulses around 1.5 μm [49]. Active f_{ceo} locking has also been demonstrated in amplified chromium lasers with intrinsic f_{ceo} detection [43] reaching a residual in-loop phase noise of 75 mrad (1 Hz–1 MHz) [35], however without achieving absolute CEP stability (i.e., $f_{ceo} = 0$). Recently, we have presented the first CEP-stable Cr:ZnS laser with 11 mrad phase noise [37], allowing precise control of the laser's waveform. Yet, the limiting factors in our CEP stabilization scheme remained to be identified, constituting a vital step toward measurements with record-high fidelity.

Here, we show an optimized and waveform-stabilized Cr:ZnS laser system that directly drives single-cycle pulse generation by exploiting nonlinear spectral broadening in a single 0.5-mm-thick bulk TiO_2 plate. We compress the super-octave-spanning pulses, extending from 1.1 to 3.1 μm, down to durations of 6.9 fs, corresponding to a single oscillation cycle of the electric field at the spectral centroid of 2.24 μm. We explore different materials for spectral broadening of chromium-doped chalcogenide lasers and identify TiO_2 as an exceptional medium in this wavelength region due to its combination of a large nonlinearity, a high bandgap, and unique dispersion properties. Numerical simulations not only closely reproduce the output spectrum of the broadening stage, but also provide detailed insights into the mechanism of spectral broadening in TiO_2. We further detect the laser f_{ceo} beating with a record-high signal-to-noise ratio of 75 dB (resolution bandwidth, RBW = 100 kHz) using a highly compact common-path f-$2f$ interferometer. The f_{ceo} signal was locked to zero, resulting in an absolute CEP stability with the residual phase noise of 5.9 mrad in the range from 0.1 Hz to 11.45 MHz—the lowest value ever shown for single- or few-cycle laser sources. Drawing on the low-noise performance of diode-pumping the oscillator, we reach a relative intensity noise (RIN) of only 0.036% (0.1 Hz–1 MHz) for the CEP-stable single-cycle output pulses. Our system is a simple and compact megahertz-rate source for single-cycle infrared pulses with unprecedented waveform stability—the ideal frontend for future field-resolved femtosecond experiments including light-wave-driven control of charge carriers [8] in low-bandgap semiconductor materials [24], and for the generation of controllable infrared waveforms spanning multiple octaves [37].

2. GENERAL SYSTEM LAYOUT

The experimental layout for the generation of single-cycle stabilized waveforms is depicted in Fig. 1. A KLM Cr^{2+}-doped ZnS laser oscillator constitutes the core of the system and delivers 540 mW of 28-fs output pulses (<4 optical cycles) at a center wavelength of 2.3 μm and a repetition rate of 22.9 MHz. The output pulses are spectrally broadened in a single TiO_2 plate, yielding 360 mW of super-octave-spanning pulses. The broadened output is split into three channels by a wedged ZnS plate, and each channel is compressed individually to single-cycle pulse durations (6.9–8.2 fs). The reflection from one of the wedge surfaces (36 mW) is sent into a common-path f-$2f$ interferometer for f_{ceo} detection. The second wedge reflection (44 mW) and the transmitted beam (230 mW) are available for downstream experiments such as mid-infrared generation with field-resolved electro-optic sampling of the generated waveforms [37].

3. DIODE-PUMPED KERR-LENS MODE-LOCKED Cr:ZnS OSCILLATOR

Direct diode pumping is the basis for the excellent intensity noise performance and CEP stability of the system. The 5-mm-long polycrystalline Cr:ZnS gain medium (IPG, anti-reflective-coated for the range 1.6–3.2 μm, 90% absorption at 1.56 μm) is pumped by two polarization-multiplexed single-emitter InP laser diodes at a wavelength of 1.65 μm ($D_{1,2}$, SemiNex), delivering together up to 4.5 W of total pump power. The nonuniform beam from the single-emitter laser diodes has strong divergence and multimode behavior along one axis and close-to-single-mode behavior along the other axis. We collimate it with a set of cylinder lenses, and focus it with a combination of an f = −200 mm meniscus lens (L_1) and an f = 80 mm achromatic lens (L_2) through the cavity mirror M_1 to a $1/e^2$-spot-size of 190 μm × 95 μm into the 5-mm-thick polycrystalline Cr:ZnS gain medium. The spot-size ratio of 2:1 optimizes the overlap volume with the intra-cavity mode [41,50].

The resonator adopts a standard, asymmetric, x-type design [43] employing two curved mirrors with f = 100 mm ($M_{1,2}$), and a 25% output coupler made of multi-layer-coated BaF_2. A 3-mm-thick MgF_2 plate, placed under Brewster's angle into the focusing cavity beam, corrects for astigmatism and favors lasing with clean

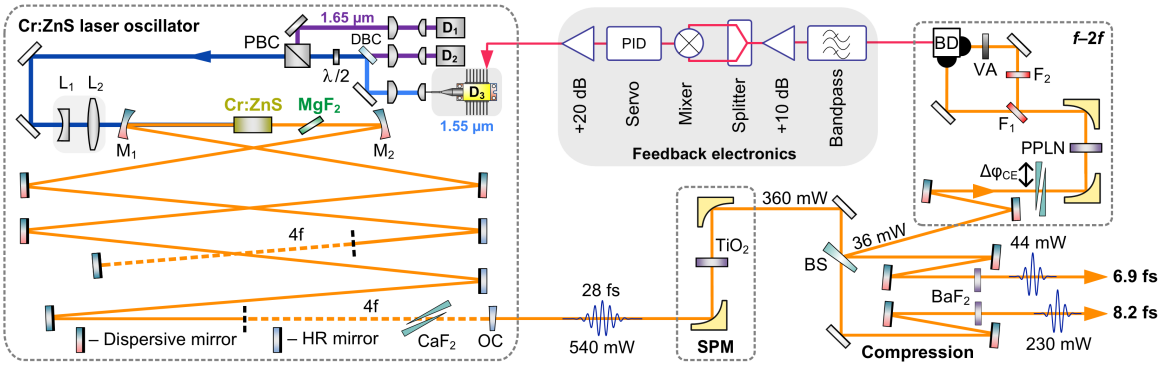

Fig. 1. Experimental setup. The diode-pumped Cr:ZnS mode-locked laser oscillator delivers 28-fs pulses, which are spectrally broadened in a thin rutile plate (TiO_2) and subsequently compressed via dispersive optics to reach single-cycle pulse durations (6.9–8.2 fs). For the f_{ceo} beat-note detection, a small fraction of the octave-spanning output is sent into a common-path f-$2f$ interferometer. By using a balanced detector, a feedback signal is provided to the modulation diode D_3 to actively control the pump diode output power. A pair of CaF_2 wedges at the f-$2f$ interferometer input enables full control over the CEP ($\Delta\varphi_{CE}$). $D_{1\text{-}3}$, pump laser diodes; DBC, dichroic beam combiner; $\lambda/2$, half-wave plate; PBC, polarizing beam combiner; L_1, meniscus lens; L_2, achromatic lens; $M_{1,2}$, curved mirrors; $4f$, $4f$-imaging telescopes for cavity extension; OC, output coupler; BS, beam splitter; PPLN, periodically poled lithium niobate crystal; $F_{1,2}$, optical filters; VA, variable attenuator; BD, balanced detector.

p polarization. For increasing the peak power, we extended the cavity round-trip path length from 6.7 to 13.1 m, corresponding to a pulse repetition rate of 22.9 MHz. For this, we elongated both short and long arms of the cavity with q-preserving $4f$-imaging telescopes consisting of two mirrors with 400-mm focal length each [51]. The oscillator is operated with a slightly negative intra-cavity dispersion, adjusted by a combination of second- and third-order dispersive mirrors, developed at our in-house coating facilities.

The CEP is stabilized by active pump-power modulation with an additional fiber-coupled single-mode laser diode (D_3, LD-PD), delivering up to 80 mW at 1.56 µm. Its output is combined with the main pump beam via a dichroic beam combiner. Long-term f_{ceo} drifts, away from the stabilized DC value, are compensated by adjusting a pair of CaF_2 wedges, placed under Brewster's angle in the resonator beam path.

The oscillator output characteristics are shown in Fig. 2. The laser provides a nearly diffraction-limited beam with an $M^2 \sim 1.1$ (see Supplement 1 Section 1), with the profile shown as an inset in Fig. 2(a). The measured pulse spectrum [black in Fig. 2(a)] covers a range from 1.95 µm (154 THz) to 2.7 µm (111 THz) at the −20-dB level. The output pulses were temporally characterized with second-harmonic frequency-resolved optical gating (SHG-FROG; see Supplement 1 Section 4). The retrieved spectrum [blue in Fig. 2(a)] matches the measured spectrum, with an almost flat phase (orange) over the full emission spectrum. The retrieved pulses [blue in Fig. 2(b)] have an intensity full width at half-maximum of 28 fs, only 1.1 times longer than the Fourier transform limit of 26 fs (FTL, black), corresponding to a peak power of 0.7 MW directly from the oscillator, considering our actual pulse shape with a shape factor of 0.79.

4. SPECTRAL BROADENING AND COMPRESSION TO SINGLE-CYCLE DURATION

Nonlinear spectral broadening in a single rutile TiO_2 plate enables further compression of the laser output to the single-cycle regime. The output beam of the Cr:ZnS oscillator is focused by a parabolic mirror (f = 15 mm) into an anti-reflective-coated TiO_2 plate [(001)-cut, CrysTec GmbH], forming a focal spot with a measured waist radius of <10 µm (limited by the resolution of our scanning-slit beam profiler). Birefringent effects due to the tetragonal crystal structure of TiO_2 were fully suppressed by placing the plate directly in the focus, with its optical axis aligned along the beam propagation axis. The output spectrum [black in Fig. 2(c)] has super-octave bandwidth, spanning from 1.1 µm (273 THz) to 3.1 µm (97 THz) at the −20-dB level with an average power of 360 mW. The spectral broadening is asymmetric around the input central wavelength of 2.3 µm (130 THz), with stronger broadening toward shorter wavelengths. Below 1.6 µm, a plateau forms, followed to shorter wavelengths by a "blue peak" around 1.2 µm [52] and a sharp roll-off. We also find a weak, broadband third harmonic [53,54]. It spans from 0.45 to 0.9 µm and does not overlap with the fundamental spectrum (see Supplement 1 Section 5). In contrast to previously reported spectral broadening in polycrystalline ZnS/ZnSe [35,43], due to rutile's centrosymmetric crystal structure we do not observe the generation of (spectrally overlapping) second-harmonic components during spectral broadening, so that the super-octave-spanning spectrum after the rutile plate is highly stable and not influenced by the driver f_{ceo}. The inset in Fig. 2(c) shows the profile of the collimated output beam. Despite the strong spectral broadening, the output beam maintains good focusing properties with M^2 values of 1.30 and 1.38 for the tangential and sagittal planes, respectively (see Supplement 1 Fig. S1). Compression of the pulses in the three channels is achieved with a single pair of dispersive mirrors each [55], combined with BaF_2 plates of variable thickness, and yielding single-cycle pulses at a spectral centroid of 2.24 µm with pulse durations between 6.9 and 8.2 fs. Note that the difference in pulse durations reflects the additional dispersion the transmitted pulses acquire from the wedged ZnS plate (see Fig. 1, BS). The amplitude and phase in the spectral and temporal domains were retrieved from SHG-FROG measurements and are shown in Figs. 2(c) and 2(d). The oscillator and spectral broadening were consistently running on a daily basis over the course of ∼1 year with only minor adjustments needed, and without any performance deterioration. These results are perfectly reproducible and consistent with our recent publication [37]. In this work, however, we focus on fully understanding the underlying broadening mechanisms.

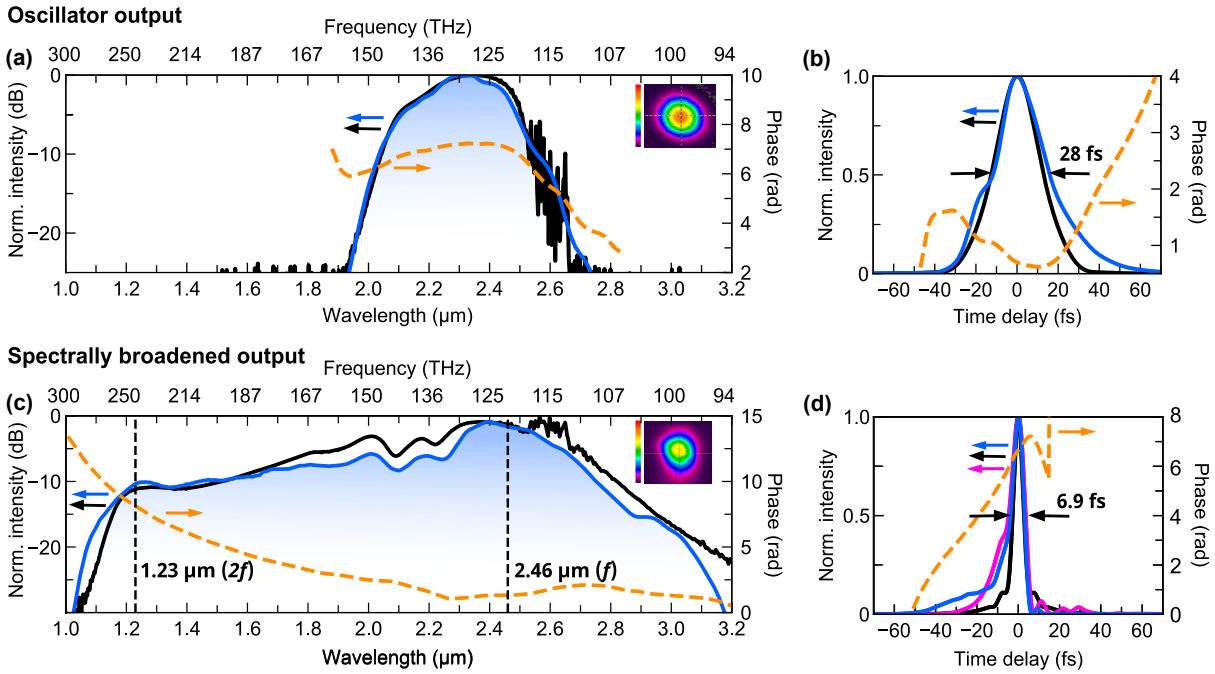

Fig. 2. Output characteristics of the laser system. (a) Spectral intensity profile (blue) and spectral phase (orange) of the oscillator output pulses, as retrieved from a measured SHG-FROG trace, shown together with the measured spectral intensity (black) and beam profile (inset, Ophir Pyrocam IIIHR). (b) Retrieved temporal profile (blue) and phase (orange) of the oscillator output, and Fourier-transform-limited pulse shown in black for comparison. (c) Spectral characteristics after nonlinear spectral broadening. Spectral intensity profile (blue) and spectral phase (orange), as retrieved from a measured SHG-FROG trace, shown together with the measured spectral intensity (black) and beam profile (inset). The positions of the f- and $2f$-components for f_{ceo} detection are highlighted. (d) Retrieved temporal profile (blue) and phase (orange) of the compressed broadband output without material in the beam, and Fourier-transform-limited pulse shown in black for comparison. The retrieved pulse transmitted through the ZnS wedge (BS, 8.2 fs; see Fig. 1) is shown in pink. The corresponding SHG-FROG traces are shown in Supplement 1 (Fig. S5).

Simulations based on the numerical solution of the nonlinear wave equation [56] complement our experimental results and provide additional insights into the broadening mechanism (Fig. 3). Since the input peak power is a factor of 2 higher than the critical power for self-focusing, multi-photon absorption and plasma formation needed to be included into the simulations [57]. The influence of these processes is experimentally confirmed by the nonlinear power loss of approximately 10%–20% accompanying the broadening process, depending on the thickness of the plate and the input peak intensity. Therefore, the nonlinear polarization comprises, in addition to the nearly instantaneous third-order susceptibility, a noninstantaneous plasma term containing both the nonlinear excitation of free carriers in the medium and their subsequent motion in the laser field (see Supplement 1 Section 3).

The above-mentioned spectral features are consistent with supercontinuum-like broadening in bulk plates [52,58–61]. Supercontinuum generation in bulk media requires a balanced interplay between self-focusing, self-phase modulation, material dispersion, and plasma generation induced by multi-photon absorption [52]. Filament formation and self-compression within the bulk plate enables the generation of ultrabroadband spectra [57,58,62,63]. With the oscillator parameters as input, the simulation reproduces the main features, bandwidth, and shape of the measured spectrum of the oscillator pulses after broadening [Fig. 3(a)]. The combination of rutile having a large nonlinear refractive index n_2 (10^{-18} m^2/W [64,65], corresponding to a large third-order susceptibility $\chi^{(3)}$) and a large optical bandgap (3–3.4 eV [66,67]), enables efficient nonlinear spectral broadening without long-term deterioration. The minimum in the group index [Fig. 3(b)], corresponding to a zero-dispersion crossing around the central wavelength, allows maintenance of group velocity matching up to the edges of the spectrum [see Fig. 3(a), around 1 and 3 μm], leading to strong spectral broadening. It is limited towards the blue by the strong increase of the group index below 1 μm.

The spectral evolution along the 0.5-mm-thick plate is shown in Fig. 3(c), complemented by the evolution of the $1/e^2$-beam radius, simulated FTL, and pulse duration in Fig. 3(d). Strongest broadening occurs after ca. 300 μm propagation inside the crystal, together with the onset of filament-like propagation, which maintains the focal spot size [orange in Fig. 3(d)] due to the interplay of self-focusing and plasma formation. Temporal self-compression due to the anomalous dispersion in the longer-wavelength part of the spectrum reduces the pulse duration [dotted blue in Fig. 3(d)], as confirmed also by SHG-FROG measurements of the direct, uncompressed output after the TiO_2 plate (Supplement 1 Fig. S6). The simultaneous spatial and temporal compression yields sustained temporal overlap over the extended interaction region of several hundreds of micrometers, resulting in a significant broadening factor and thus reduction of the FTL [dashed pink in Fig. 3(d)] at relatively low pulse energies. Higher-order dispersion becomes dominant at longer propagation distances. Using a 500-μm-thick rutile plate provides in our case the optimum compromise between spectral broadening and accumulation of higher-order dispersion. The thin medium and strong focusing conditions also allow avoiding spatial beam degradation, as typically observed for strong nonlinear broadening in bulk media [68]. Self-focusing and the resulting filament-like propagation

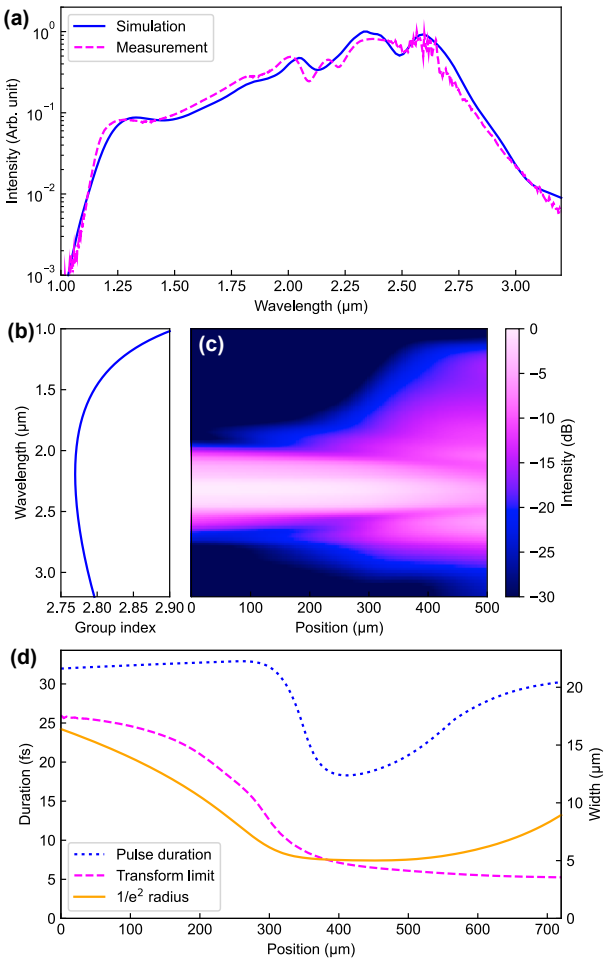

Fig. 3. Nonlinear simulations of spectral broadening in rutile. (a) Simulated output spectrum (blue curve) as obtained from nonlinear spectral broadening of the oscillator pulses in a 0.5-mm-thick (001)-orientated rutile plate in comparison to the experimental spectrum (dashed pink curve). (b) Group refractive index as a function of wavelength in the medium. (c) Evolution of the spectrum as a function of propagation distance in the medium. (d) Comparison of the spatial evolution of the pulse duration, Fourier transform limit of the corresponding spectrum, and the beam radius as the pulse propagates through the rutile plate. The total interaction results from the interplay of spatial and temporal self-compression, combined with the sustained temporal overlap of the wings of the spectrum.

homogenizes the spatial distribution of the spectral components. Degradation of the beam quality is thus minimized [57,69,70], explaining our M^2 values < 1.4 for the spectrally broadened beam.

5. EXPLORING OTHER MATERIALS FOR SPECTRAL BROADENING

We tested a variety of alternative materials for spectral broadening of chromium-doped chalcogenide lasers in a single thin plate and recorded the blue part of the output spectra between 0.8 and 2.6 μm for different uncoated media under strong focusing conditions [Fig. 4(a)]. Except for ZnS and ZnSe, the materials were chosen such that they have a zero-crossing of the group velocity dispersion (GVD) close to the center wavelength of the oscillator output [Fig. 4(b)] and a sufficiently large nonlinear refractive index or third-order susceptibility (Table 1) to enable spectral broadening (see Supplement 1 Section 2). ZnS and ZnSe feature a positive dispersion across the relevant wavelength range but have a large nonlinear refractive index around 2.3 μm giving rise to strong spectral broadening in the positive dispersion regime [43,77].

Table 1. Summary of the Dispersion Zero-Crossings and Third-Order Susceptibilities for the Investigated Materials[a]

Material	Dispersion Zero-Crossing (μm)	Third-Order Susceptibility $\chi^{(3)}$ (m^2/V^2)
TiO_2 (001)	2.27	$2.65 \cdot 10^{-20}$ (from simulation)
$SrTiO_3$	2.05	$0.91 \cdot 10^{-20}$ [72] / $2.40 \cdot 10^{-20}$ (from simulation)
ZrO_2	1.85	$6.29 \cdot 10^{-21}$ [73]
ZnSe	4.80	$1.28 \cdot 10^{-20}$ [74]
ZnS	3.60	$5.74 \cdot 10^{-21}$ [74]
GaN	2.23	$2.28 \cdot 10^{-20}$ [75]
PbF_2	2.48	$1.25 \cdot 10^{-21}$ [76]

[a]The zero-crossings of the material dispersion curves are extracted from Fig. 4(b). Note that the third-order susceptibility $\chi^{(3)}$ is directly proportional to the nonlinear refractive index n_2 [71].

Compared to TiO_2 in (001)-orientation [black curve in Fig. 4(a)], all tested materials exhibit significantly weaker or only minor spectral broadening under our experimental conditions. In addition to spectral broadening, ZnS and ZnSe show pronounced second-harmonic generation in the range 1.0 to 1.3 μm due to random quasi-phase-matching (RQPM) in the polycrystalline materials [78]. Previously reported chromium-based laser systems used the simultaneous broadening and generation of overlapping harmonics to generate a beating signal for f_{ceo} stabilization [35,43]. TiO_2 does not generate any second-harmonic component that would overlap and interfere with the fundamental spectrum (1.1 to 3.1 μm). Therefore, we can favorably separate spectral broadening and CEP stabilization, and optimize both individually to highest levels. As additional drawbacks for ZnS and ZnSe, we observed nonreversible degradation of the samples under our experimental conditions over the duration of several hours, while rutile has remained stable under supercontinuum-generation conditions over the duration of more than 1 year without any degradation.

In order to better understand the fundamental differences in the experimentally tested materials, numerical simulations were performed on $SrTiO_3$ and ZnSe as representative materials, for which sufficient literature data was available (see Supplement 1 Section 6). We examined $SrTiO_3$ as a nonbirefringent alternative to TiO_2 with a zero-crossing of the GVD close to the center wavelength of the driving pulse [Fig. 4(b)]. The simulations for the (100) orientation reproduce the broadening behavior and allow further insight into their differences with the more effective process in TiO_2. In terms of the underlying physical effects, $SrTiO_3$ supports the same broadening mechanisms governed by self-focusing and self-compression as TiO_2. However, it does not reach as large of a spectral bandwidth due to a combination of a slightly lower third-order susceptibility, higher nonlinear absorption, and higher dispersion. This combination of factors prevents the beam from reaching the level of spatiotemporal confinement observed in TiO_2 using the present laser system. In contrast to TiO_2 and $SrTiO_3$,

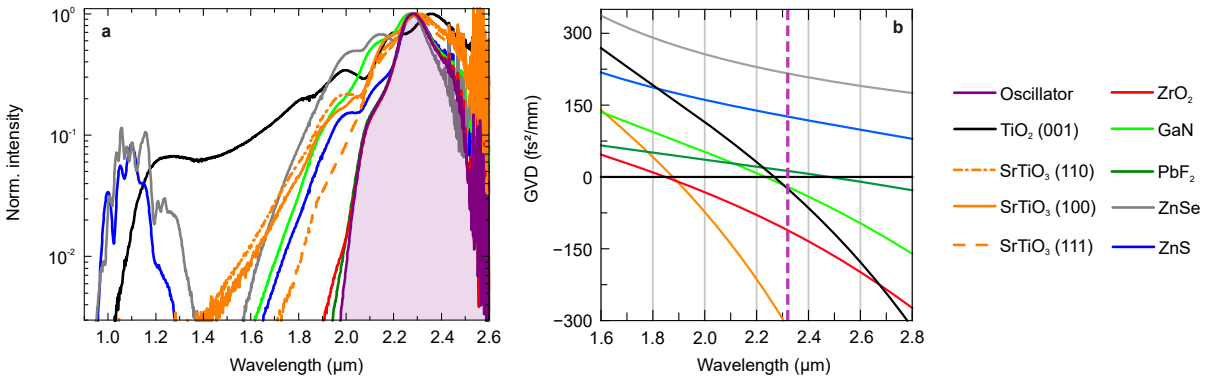

Fig. 4. Group velocity dispersion (GVD) and corresponding spectra of the tested material plates under strong focusing conditions. (a) Measured spectra for different broadening materials. Except for ZnS and ZnSe, the materials were chosen to feature a zero-crossing of the dispersion close to the center wavelength of the driving laser. All plates were uncoated and 0.5 mm thick, except for GaN (0.335 mm thickness). Pronounced second-harmonic generation was observed for ZnS and ZnSe due to random quasi-phase-matching in the polycrystalline materials. (b) The GVD calculations are based on the Sellmeier coefficients extracted from the refractive index database [79], except for $SrTiO_3$ which was taken from [80]. The dashed vertical line marks the central wavelength of our laser oscillator pulses.

ZnSe and ZnS have GVD zero transitions beyond 3 μm. The strong positive GVD over the pulse's spectral range prevents a similar form of self-compression as compared to TiO_2. In exemplary simulations on ZnSe we find that the dynamics differ more drastically from TiO_2 than expected from the GVD alone. Due to the above-mentioned buildup of the second-harmonic signal allowed by RQPM in the polycrystalline material [78] the broadening mechanism has a strong contribution from a cascaded second-order nonlinearity in addition to the underlying third-order susceptibility. This additional contribution allows significant broadening despite the large positive dispersion in this wavelength range, albeit at the expense of spatiotemporal distortion during propagation.

In summary, our experimental results and simulations single out rutile (TiO_2) in (001)-orientation as an exceptional broadening medium due to its large output bandwidth without contamination by overlapping harmonics, and due to its outstanding long-term stability.

6. CARRIER-ENVELOPE PHASE STABILIZATION

CEP stabilization of the Cr:ZnS laser locks the waveform of the single-cycle output pulses. We detected the carrier-envelope-offset frequency (f_{ceo}) with a common-path f-$2f$ interferometer and achieved full CEP stabilization with a self-referenced locking concept [81], combined with pump-power modulation (via diode D_3 in Fig. 1) of the oscillator.

Interferometric f_{ceo} detection is driven by 36 mW of the compressed, single-cycle pulses, focused with an off-axis parabolic mirror (f = 25.4 mm) into a 2-mm-thick, periodically poled lithium niobate crystal (HC Photonics). The crystal is used for second-harmonic generation of a spectral component around 2.46 μm. The resulting frequency-doubled components interfere with the fundamental ones at 1.23 μm [dashed black lines in Fig. 2(c)]. The interfering spectral components are isolated with a 30-nm-wide optical bandpass filter (F_1, Semrock), and sent onto one of the photodiodes of a low-noise balanced detector for beat-note detection (BD, HBPR-100M-60 K-IN; Femto). The repetition-rate signal f_{rep} is partially canceled by sending the beam reflected from F_1, through a 1.5-μm long-pass filter (F_2, Thorlabs), onto the second photodiode of the BD. A variable attenuator adjusts the balancing to achieve optimum residual phase noise for the feedback lock. The radio-frequency power spectrum of the detected signal [Fig. 5(a)] shows f_{ceo} and $f_{rep} \pm f_{ceo}$ beat notes with a record-high signal-to-noise ratio (SNR) of ∼75 dB at a 100-kHz resolution bandwidth. Additional lower-intensity intermodulation signals arise from saturation effects in the BD, preventing the measurement of even stronger beat notes. This issue can be avoided in the future with higher-dynamic-range detectors. The achieved SNR exceeds by 15 dB any previously published works [37,82–84]. It is the result of several favorable aspects of our system. First, efficient spectral broadening and second-harmonic generation provide a large number of photons (60 μW of average power after F_1) within the detected frequency band of the f-$2f$ beating signal. Moreover, when compared to spectral broadening based in photonic crystal fibers [85,86], our single-cycle pulses from bulk broadening feature excellent phase coherence and intrinsic temporal overlap of f and $2f$ components without additional path-length correction.

The electronic feedback signal for CEP locking is generated by mixing the $f_{rep} \pm f_{ceo}$ beat notes with each other [81]. For this, the output of the BD is bandpass-filtered around f_{rep} (BBP −21.4+; Mini-Circuits), amplified by +10 dB (DHPVA-101; Femto) and divided with a 50:50 splitter into two equal radio-frequency signals, which are then sent to a double-balanced mixer (ZAD-1 H+; Mini-Circuits) to generate the error signal for the feedback loop. The output is sent into a proportional–integral–derivative servo (PID, D2-125; Vescent) to modulate the current of the pump diode D_3 after +20-dB post-amplification (HVA-500M-20-B; Femto).

The diode D_3 is driven by an in-house-developed, digitally controlled driver with integrated thermo-electric cooling. When compared with the driver employed in [37], here we developed an entirely new unit with significantly improved performance. The two key features regarding our application are low-noise operation and fast modulation. The upgraded unit features a current stability of 8 ppm/K, and a current noise density of only 5 nA · $Hz^{-1/2}$ at 1 kHz. The integrated current noise has been improved five-fold (down to 3.3 μA), and the modulation bandwidth has been increased by a factor of 4, to 1.2 MHz (see Supplement 1 Section 7). At this frequency, the phase-transfer function [red in

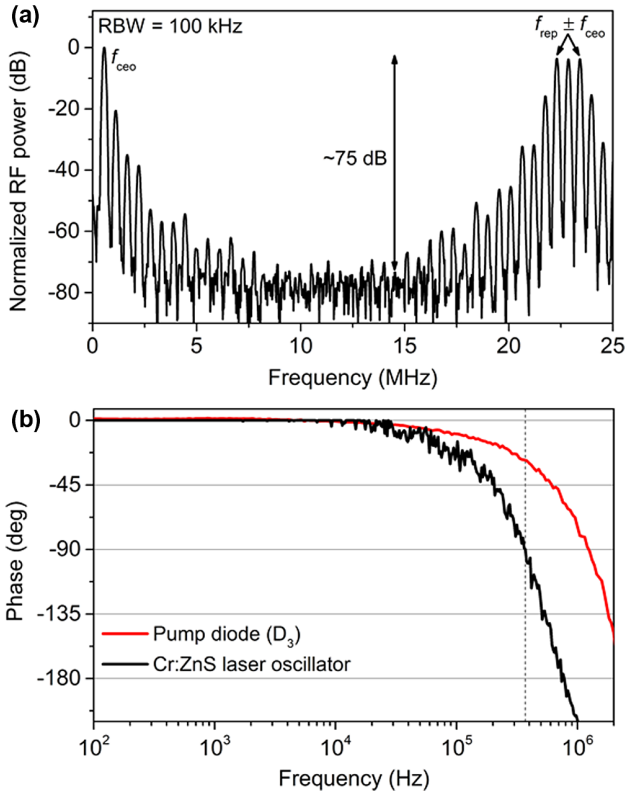

Fig. 5. (a) Radio-frequency power spectrum showing the measured f_{ceo} and f_{rep} signals and their mixing terms for the free-running laser system (measurement resolution bandwidth, RBW = 100 kHz). (b) Phase transfer function for the modulation pump diode D_3 (red) and the Cr:ZnS laser oscillator (black). The dashed vertical line indicates a 90° phase lag of the Cr:ZnS oscillator with respect to the applied modulation.

Fig. 5(b)] reaches a critical lag of 90 deg. For the mode-locked Cr:ZnS laser oscillator [black in Fig. 5(b)], modulated by the diode D_3, the cutoff frequency of the phase transfer function amounts to approximately 370 kHz, as a result of fluorescence-lifetime (~4.3 μs [87]) filtering by the gain medium. Thus, it constitutes the main limitation regarding the modulation bandwidth in our setup. Drifts of f_{ceo} outside the ~10 kHz control range of the pump modulation are corrected by moving the intra-cavity CaF_2 wedges (Fig. 1). The main contributions to slow f_{ceo} variations were changes of the relative humidity inside the oscillator chamber, in agreement with previously published observations [35]. The CEP of the locked oscillator output can be adjusted, without any additional dispersion in the main beam path, by changing the CEP of the pulses sent to the f-$2f$ interferometer with a pair of CaF_2 wedges (Fig. 1).

7. NOISE PERFORMANCE OF THE SYSTEM

The RIN of the spectrally broadened, single-cycle output pulses is shown in Fig. 6(a) both for the free-running and the CEP-stabilized system (see Supplement 1 Section 8). The RIN of the free-running oscillator [black in Fig. 6(a)] agrees with the results from previous publications on diode-pumped Cr:ZnS oscillators [37,40]: the low-frequency RIN shows typical $1/f$ noise up to 100 Hz, and some spikes from mechanical vibrations and electrical noise above that. In the range between 300 Hz to 300 kHz a plateau region is observed, dominated by diode-pump noise [40], and followed by a relaxation oscillation bump [34] at around 300 kHz. At frequencies above 1 MHz, the RIN drops to the detection noise level, due to the intrinsic fluorescence-lifetime low-pass filtering of the Cr:ZnS gain medium, so that we have chosen this frequency as the upper limit for the RIN integration [40]. The RMS intensity noise measured in the range 0.1 Hz–1 MHz amounts to 0.039% [dashed red in Fig. 6(a)]. We attribute the excellent stability mainly to the low-noise performance of diode pumping. In contrast to typically used Er:fiber lasers [32,34,88], semiconductor laser diodes have relaxation oscillation noise in the gigahertz regime, beyond the response of the Cr:ZnS gain medium. Additional noise dampening occurs due to intra-cavity second-harmonic generation in the polycrystalline gain medium [89]. CEP stabilization of the oscillator reduces the RIN in the plateau region [300 Hz–300 kHz, blue in Fig. 6(a)], as the stabilization partially compensates residual pump power fluctuations. Simultaneously, a servo bump appears at 450 kHz, due to the interplay of the CEP stabilization feedback loop with the oscillator gain dynamics. The integrated RIN of the CEP-stabilized laser yields an RMS noise value of only 0.036 % in the frequency range 0.1 Hz to 1 MHz [dashed orange in Fig. 6(a)].

The CEP stability was quantified with a separate out-of-loop f-$2f$ interferometer in the main output beam of the system (see Supplement 1 Section 9). The residual phase noise power spectral density [blue in Fig. 6(b)] mimics the appearance of the RIN curve [blue in Fig. 6(a)], and we find an RMS phase noise of only 5.9 mrad (phase jitter of 6.8 fs at 2.2 μm), when integrating over all 8 frequency decades, from 0.1 Hz up to the Nyquist limit of 11.45 MHz (with 2.4 mrad measurement floor limit; gray).

This remarkably high CEP stability is the result of a combination of several key features of our system: (i) the intrinsic low-intensity-noise performance of the free-running oscillator due to direct diode pumping, which is directly coupled to the phase stability [83]; (ii) employing a single rutile plate for spectral broadening, rather than highly nonlinear optical fibers, enabled a common-path design of the f-$2f$ interferometer with minimized drifts, optimal temporal overlap and undisturbed pulse coherence [85,86], enabling us to reach an unprecedented f_{ceo} SNR of 75 dB; and (iii) an optimum feedback into the oscillator by modulating the diode D_3 with our custom-developed, fast, and low-noise diode driver.

Compared to [37], our advanced CEP stabilization is not any more limited by the bandwidth of the locking electronics, but by the intrinsic lifetime of the Cr:ZnS gain medium and the related relaxation oscillation (servo bump at ~450 kHz). We estimate a fundamental limit on the integrated phase noise reachable with our f_{ceo} beat-note SNR to be ~1.8 mrad [82], and our feedback loop allows us to approach this value within a factor of only 3.3.

Our residual CEP noise is an order of magnitude lower than previous results based on intrinsic interferometry in a Cr:ZnS amplifier crystal [35] and twice better than our previously published results [37]. Moreover, it represents the highest CEP stability ever achieved with a direct feedback locking [83,84], and the highest stability in general for sources producing single- or few-cycle pulses [22,90,91]. Finally, it approaches the lowest CEP jitter for any mode-locked laser obtained with a feed-forward technique [49]. When compared with the latter, our approach does not require an acousto-optic modulator, and thus avoids additional losses as well as material and angular dispersion imposed on the laser beam, which impair the use of a feed-forward technique for ultrabroadband laser sources.

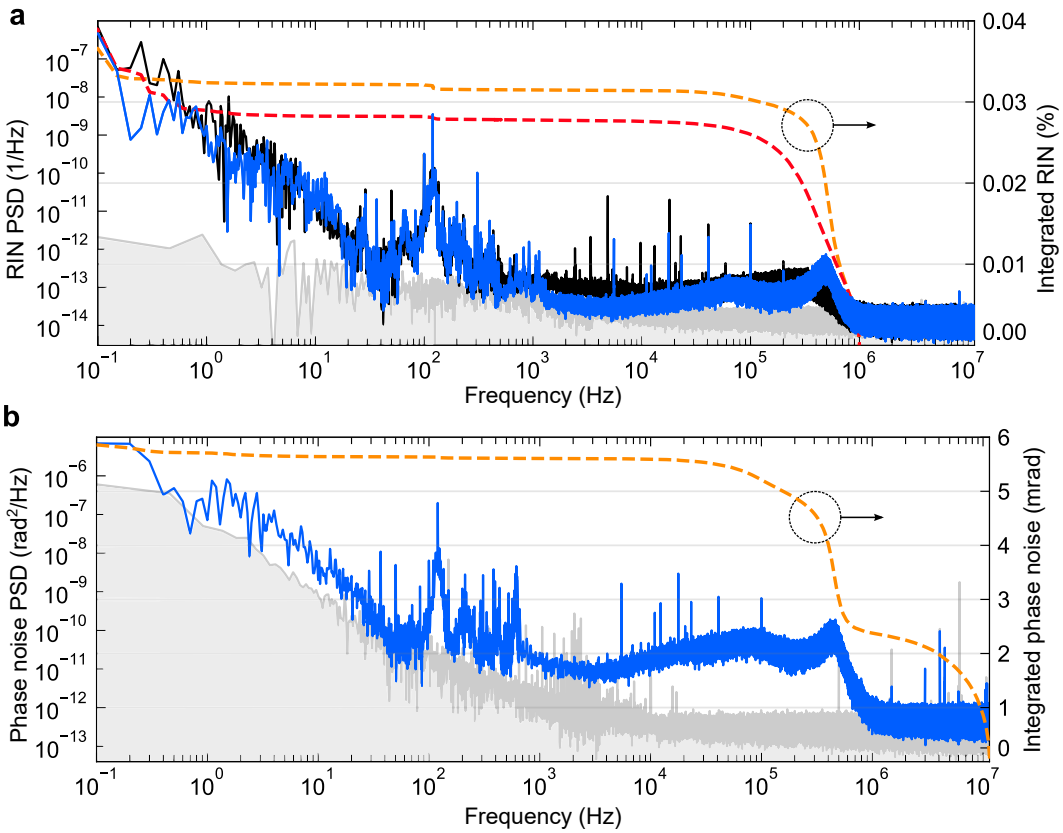

Fig. 6. Noise performance of the system. (a) Relative intensity noise power spectral density (solid line) and the corresponding integrated noise (dashed) of the free-running (black, red) and the CEP-stabilized laser (blue, orange). (b) CEP noise power spectral density (blue) and the corresponding integrated phase noise of the stabilized laser (orange). The detection noise levels for the two measurement setups are shown in gray.

8. CONCLUSIONS

We have reported a new source for highly CEP-stable single-cycle pulses centered around 2.2 μm. The simple and compact system is based on a directly diode-pumped Cr:ZnS oscillator with subsequent supercontinuum generation in a single 0.5-mm-thick rutile (TiO_2) plate. It provides two output channels (44 mW and 230 mW) with super-octave-spanning pulses, covering a spectral range from 1.1 to 3.1 μm (−20-dB level), compressed to single-cycle durations of 6.9 fs and 8.2 fs. We explored various alternative bulk materials for spectral broadening of chromium-doped chalcogenide lasers and assigned the exceptional performance of rutile to a combination of its high nonlinear refractive index, large optical bandgap, and favorable group-delay dispersion with a zero-crossing in the spectral center of the driving pulse. Numerical simulations of the broadening process quantitatively reproduce the supercontinuum spectrum and identify a dynamic interplay between self-phase modulation, self-focusing, and plasma formation as the main underlying processes [56]. We actively stabilized the CEP of the output pulses by combining, in a feedback loop, beat-note detection in a common-path f-$2f$ interferometer with a record-high 75 dB SNR, and low-noise pump-power modulation. The single-cycle output pulses of our system are highly waveform-stable, featuring a unique combination of excellent amplitude stability (0.036% RIN in the 0.1 Hz–1 MHz range) and unprecedented phase stability for single- or few-cycle laser systems (5.9 mrad residual CEP noise in the 0.1 Hz–11.45 MHz range).

The highly reproducible single-cycle infrared pulses from our system provide new tools for the precise, megahertz-rate control of the nonlinear polarization in matter on the inherent, sub-femtosecond time scale of the electric-field evolution. Possible experiments include the field-driven control of electron motion in molecules [4] and solids [5,8,17], and high-harmonic generation in enhancement cavities [92]. The single-cycle output pulses can be further converted efficiently into multi-octave spanning mid-infrared pulses with CEP-controllable waveforms [37], opening up new applications in mid-infrared field-resolved biosensing [93] and the manipulation of currents in low-bandgap materials [24]. Our approach to infrared single-cycle pulses is power-scalable by optically amplifying the oscillator output before spectral broadening [40]. With precise numerical simulations of the spectral broadening now available, we expect to be able to tailor the experimental conditions further to extend the spectral bandwidth toward the visible. Together with field-synthesis techniques [94] the generation of controllable sub-cycle pulses from megahertz-rate Cr:ZnS oscillators will come into reach.

Funding. Centre for Advanced Laser Applications; Ludwig-Maximilians-Universität München; Max-Planck-Institut für Quantenoptik; Center for Molecular Fingerprinting Research (CMF).

Acknowledgment. M. K. acknowledges Günter Steinmeyer (Max Born Institute for Nonlinear Optics and Short Pulse Spectroscopy) and Łukasz Sterczewski (Wrocław University of Science and Technology) for their assistance on estimating the fundamental limits of CEP stabilization. A. G. and A. H. thank the 'NLPQT—National Laboratory for Photonics and Quantum Technologies' (Poland) for providing the test equipment to evaluate the diode driver performance.

Disclosures. M. K., N. N., P. S., F. K., K. M., and A. W. have filed patent application(s) on some aspects of the presented work. The remaining authors declare no conflicts of interest.

Data availability. Data underlying the results presented in this paper are not publicly available at this time but may be obtained from the authors upon reasonable request.

Supplemental document. See Supplement 1 for supporting content.

REFERENCES

1. M. Hentschel, R. Kienberger, C. Spielmann, G. A. Reider, N. Milosevic, T. Brabec, P. Corkum, U. Heinzmann, M. Drescher, and F. Krausz, "Attosecond metrology," Nature **414**, 509–513 (2001).
2. F. Krausz and M. Ivanov, "Attosecond physics," Rev. Mod. Phys. **81**, 163–234 (2009).
3. A. Sommer, E. M. Bothschafter, S. A. Sato, C. Jakubeit, T. Latka, O. Razskazovskaya, H. Fattahi, M. Jobst, W. Schweinberger, V. Shirvanyan, V. S. Yakovlev, R. Kienberger, K. Yabana, N. Karpowicz, M. Schultze, and F. Krausz, "Attosecond nonlinear polarization and light–matter energy transfer in solids," Nature **534**, 86–90 (2016).
4. M. F. Kling, C. Siedschlag, A. J. Verhoef, J. I. Khan, M. Schultze, T. Uphues, Y. Ni, M. Uiberacker, M. Drescher, F. Krausz, and M. J. J. Vrakking, "Control of electron localization in molecular dissociation," Science **312**, 246–248 (2006).
5. A. Schiffrin, T. Paasch-Colberg, N. Karpowicz, V. Apalkov, D. Gerster, S. Mühlbrandt, M. Korbman, J. Reichert, M. Schultze, S. Holzner, J. V. Barth, R. Kienberger, R. Ernstorfer, V. S. Yakovlev, M. I. Stockman, and F. Krausz, "Optical-field-induced current in dielectrics," Nature **493**, 70–74 (2013).
6. G. Vampa, T. J. Hammond, M. Taucer, X. Ding, X. Ropagnol, T. Ozaki, S. Delprat, M. Chaker, N. Thiré, B. E. Schmidt, F. Légaré, D. D. Klug, A. Y. Naumov, D. M. Villeneuve, A. Staudte, and P. B. Corkum, "Strong-field optoelectronics in solids," Nat. Photonics **12**, 465–468 (2018).
7. F. Schlaepfer, M. Lucchini, S. A. Sato, M. Volkov, L. Kasmi, N. Hartmann, A. Rubio, L. Gallmann, and U. Keller, "Attosecond optical-field-enhanced carrier injection into the GaAs conduction band," Nat. Phys. **14**, 560–564 (2018).
8. T. Boolakee, C. Heide, A. Garzón-Ramírez, H. B. Weber, I. Franco, and P. Hommelhoff, "Light-field control of real and virtual charge carriers," Nature **605**, 251–255 (2022).
9. S. Sederberg, D. Zimin, S. Keiber, F. Siegrist, M. S. Wismer, V. S. Yakovlev, I. Floss, C. Lemell, J. Burgdörfer, M. Schultze, F. Krausz, and N. Karpowicz, "Attosecond optoelectronic field measurement in solids," Nat. Commun. **11**, 430 (2020).
10. M. R. Bionta, F. Ritzkowsky, M. Turchetti, Y. Yang, D. Cattozzo Mor, W. P. Putnam, F. X. Kärtner, K. K. Berggren, and P. D. Keathley, "On-chip sampling of optical fields with attosecond resolution," Nat. Photonics **15**, 456–460 (2021).
11. Y. Liu, J. E. Beetar, J. Nesper, S. Gholam-Mirzaei, and M. Chini, "Single-shot measurement of few-cycle optical waveforms on a chip," Nat. Photonics **16**, 109–112 (2022).
12. M. Seo, K. Tsendsuren, S. Mitra, M. Kling, and D. Kim, "High-contrast, intense single-cycle pulses from an all thin-solid-plate setup," Opt. Lett. **45**, 367–370 (2020).
13. M.-S. Tsai, A.-Y. Liang, C.-L. Tsai, P.-W. Lai, M.-W. Lin, and M.-C. Chen, "Nonlinear compression toward high-energy single-cycle pulses by cascaded focus and compression," Sci. Adv. **8**, eabo1945 (2022).
14. T. Balciunas, C. Fourcade-Dutin, G. Fan, T. Witting, A. A. Voronin, A. M. Zheltikov, F. Gerome, G. G. Paulus, A. Baltuska, and F. Benabid, "A strong-field driver in the single-cycle regime based on self-compression in a Kagome fibre," Nat. Commun. **6**, 6117 (2015).
15. J. C. Travers, T. F. Grigorova, C. Brahms, and F. Belli, "High-energy pulse self-compression and ultraviolet generation through soliton dynamics in hollow capillary fibres," Nat. Photonics **13**, 547–554 (2019).
16. I. V. Savitsky, E. A. Stepanov, A. A. Lanin, A. B. Fedotov, and A. M. Zheltikov, "Single-cycle, multigigawatt carrier–envelope-phase-tailored near-to-mid-infrared driver for strong-field nonlinear optics," ACS Photonics **9**, 1679–1690 (2022).
17. T. Rybka, M. Ludwig, M. F. Schmalz, V. Knittel, D. Brida, and A. Leitenstorfer, "Sub-cycle optical phase control of nanotunnelling in the single-electron regime," Nat. Photonics **10**, 667–670 (2016).
18. W. P. Putnam, R. G. Hobbs, P. D. Keathley, K. K. Berggren, and F. X. Kärtner, "Optical-field-controlled photoemission from plasmonic nanoparticles," Nat. Phys. **13**, 335–339 (2017).
19. V. Hanus, V. Csajbók, Z. Pápa, J. Budai, Z. Márton, G. Z. Kiss, P. Sándor, P. Paul, A. Szeghalmi, Z. Wang, B. Bergues, M. F. Kling, G. Molnár, J. Volk, and P. Dombi, "Light-field-driven current control in solids with pJ-level laser pulses at 80 MHz repetition rate," Optica **8**, 570–576 (2021).
20. D. J. Jones, S. A. Diddams, J. K. Ranka, A. Stentz, R. S. Windeler, J. L. Hall, and S. T. Cundiff, "Carrier-envelope phase control of femtosecond mode-locked lasers and direct optical frequency synthesis," Science **288**, 635–639 (2000).
21. U. Morgner, F. X. Kärtner, S. H. Cho, Y. Chen, H. A. Haus, J. G. Fujimoto, E. P. Ippen, V. Scheuer, G. Angelow, and T. Tschudi, "Sub-two-cycle pulses from a Kerr-lens mode-locked Ti:sapphire laser," Opt. Lett. **24**, 411–413 (1999).
22. S. Rausch, T. Binhammer, A. Harth, J. Kim, R. Ell, F. X. Kärtner, and U. Morgner, "Controlled waveforms on the single-cycle scale from a femtosecond oscillator," Opt. Express **16**, 9739–9745 (2008).
23. M. P. Fischer, N. Maccaferri, K. Gallacher, J. Frigerio, G. Pellegrini, D. J. Paul, G. Isella, A. Leitenstorfer, P. Biagioni, and D. Brida, "Field-resolved detection of the temporal response of a single plasmonic antenna in the mid-infrared," Optica **8**, 898–903 (2021).
24. M. T. Schlecht, M. Knorr, C. P. Schmid, S. Malzer, R. Huber, and H. B. Weber, "Light-field-driven electronics in the mid-infrared regime: Schottky rectification," Sci. Adv. **8**, eabj5014 (2022).
25. G. Krauss, S. Lohss, T. Hanke, A. Sell, S. Eggert, R. Huber, and A. Leitenstorfer, "Synthesis of a single cycle of light with compact erbium-doped fibre technology," Nat. Photonics **4**, 33–36 (2010).
26. C. Schoenfeld, P. Sulzer, D. Brida, A. Leitenstorfer, and T. Kurihara, "Passively phase-locked Er:fiber source of single-cycle pulses in the near infrared with electro-optic timing modulation for field-resolved electron control," Opt. Lett. **47**, 3552–3555 (2022).
27. S. Xing, D. M. B. Lesko, T. Umeki, A. J. Lind, N. Hoghooghi, T.-H. Wu, and S. A. Diddams, "Single-cycle all-fiber frequency comb," APL Photonics **6**, 086110 (2021).
28. I. T. Sorokina, "Cr^{2+}-doped II–VI materials for lasers and nonlinear optics," Opt. Mater. **26**, 395–412 (2004).
29. I. T. Sorokina, E. Sorokin, and T. J. Carrig, "Femtosecond pulse generation from a SESAM mode-locked Cr:ZnSe laser," in *Conference on Lasers and Electro-Optics/Quantum Electronics and Laser Science Conference and Photonic Applications Systems Technologies* (Optica Publishing Group, 2006), paper CMQ2.
30. M. N. Cizmeciyan, H. Cankaya, A. Kurt, and A. Sennaroglu, "Kerr-lens mode-locked femtosecond Cr^{2+}:ZnSe laser at 2420 nm," Opt. Lett. **34**, 3056–3058 (2009).
31. M. N. Cizmeciyan, J. W. Kim, S. Bae, B. H. Hong, F. Rotermund, and A. Sennaroglu, "Graphene mode-locked femtosecond Cr:ZnSe laser at 2500 nm," Opt. Lett. **38**, 341–343 (2013).
32. S. B. Mirov, I. S. Moskalev, S. Vasilyev, V. Smolski, V. V. Fedorov, D. Martyshkin, J. Peppers, M. Mirov, A. Dergachev, and V. Gapontsev, "Frontiers of mid-IR lasers based on transition metal doped chalcogenides," IEEE J. Sel. Top. Quantum Electron. **24**, 1601829 (2018).
33. N. Nagl, S. Gröbmeyer, V. Pervak, F. Krausz, O. Pronin, and K. F. Mak, "Directly diode-pumped, Kerr-lens mode-locked, few-cycle Cr:ZnSe oscillator," Opt. Express **27**, 24445–24454 (2019).
34. A. Barh, B. Ö. Alaydin, J. Heidrich, M. Gaulke, M. Golling, C. R. Phillips, and U. Keller, "High-power low-noise 2-GHz femtosecond laser oscillator at 2.4 μm," Opt. Express **30**, 5019–5025 (2022).
35. S. Vasilyev, V. Smolski, J. Peppers, I. Moskalev, M. Mirov, Y. Barnakov, S. Mirov, and V. Gapontsev, "Middle-IR frequency comb based on Cr:ZnS laser," Opt. Express **27**, 35079–35087 (2019).
36. S. Vasilyev, I. S. Moskalev, V. O. Smolski, J. M. Peppers, M. Mirov, A. V. Muraviev, K. Zawilski, P. G. Schunemann, S. B. Mirov, K. L. Vodopyanov, and V. P. Gapontsev, "Super-octave longwave mid-infrared coherent transients produced by optical rectification of few-cycle 2.5-μm pulses," Optica **6**, 111–114 (2019).
37. P. Steinleitner, N. Nagl, M. Kowalczyk, J. Zhang, V. Pervak, C. Hofer, A. Hudzikowski, J. Sotor, A. Weigel, F. Krausz, and K. F. Mak, "Single-cycle infrared waveform control," Nat. Photonics **16**, 512–518 (2022).
38. V. E. Leshchenko, B. K. Talbert, Y. H. Lai, S. Li, Y. Tang, S. J. Hageman, G. Smith, P. Agostini, L. F. DiMauro, and C. I. Blaga, "High-power few-cycle

Cr:ZnSe mid-infrared source for attosecond soft x-ray physics," Optica **7**, 981–988 (2020).
39. N. Nagl, S. Gröbmeyer, M. Pötzlberger, V. Pervak, F. Krausz, and K. F. Mak, "Directly diode-pumped few-optical-cycle Cr:ZnS Laser at 800 mW of average power," in *Conference on Lasers and Electro-Optics* (Optical Society of America, 2020), paper SF3H.5.
40. S. Qu, A. Paudel, A. Sebesta, P. Steinleitner, N. Nagl, M. Poetzlberger, V. Pervak, K. F. Mak, and A. Weigel, "Directly diode-pumped femtosecond Cr:ZnS amplifier with ultra-low intensity noise," Opt. Lett. **47**, 6217–6220 (2022).
41. N. Nagl, *A New Generation of Ultrafast Oscillators for Mid-Infrared Applications* (Springer, 2022).
42. S. Vasilyev, I. Moskalev, M. Mirov, V. Smolski, S. Mirov, and V. Gapontsev, "Ultrafast middle-IR lasers and amplifiers based on polycrystalline Cr:ZnS and Cr:ZnSe," Opt. Mater. Express **7**, 2636–2650 (2017).
43. S. Vasilyev, I. Moskalev, V. Smolski, J. Peppers, M. Mirov, V. Fedorov, D. Martyshkin, S. Mirov, and V. Gapontsev, "Octave-spanning Cr:ZnS femtosecond laser with intrinsic nonlinear interferometry," Optica **6**, 126–127 (2019).
44. N. Nagl, K. Mak, Q. Wang, V. Pervak, F. Krausz, and O. Pronin, "Efficient femtosecond mid-infrared generation based on a Cr:ZnS oscillator and step-index fluoride fibers," Opt. Lett. **44**, 2390–2393 (2019).
45. A. Baltuška, T. Fuji, and T. Kobayashi, "Controlling the carrier-envelope phase of ultrashort light pulses with optical parametric amplifiers," Phys. Rev. Lett. **88**, 133901 (2002).
46. U. Elu, M. Baudisch, H. Pires, F. Tani, M. H. Frosz, F. Köttig, A. Ermolov, P. St.J. Russell, and J. Biegert, "High average power and single-cycle pulses from a mid-IR optical parametric chirped pulse amplifier," Optica **4**, 1024–1029 (2017).
47. H. R. Telle, G. Steinmeyer, A. E. Dunlop, J. Stenger, D. H. Sutter, and U. Keller, "Carrier-envelope offset phase control: a novel concept for absolute optical frequency measurement and ultrashort pulse generation," Appl. Phys. B **69**, 327–332 (1999).
48. S. Koke, C. Grebing, H. Frei, A. Anderson, A. Assion, and G. Steinmeyer, "Direct frequency comb synthesis with arbitrary offset and shot-noise-limited phase noise," Nat. Photonics **4**, 462–465 (2010).
49. R. Lemons, W. Liu, I. F. de Fuentes, S. Droste, G. Steinmeyer, C. G. Durfee, and S. Carbajo, "Carrier-envelope phase stabilization of an Er:Yb:glass laser via a feed-forward technique," Opt. Lett. **44**, 5610–5613 (2019).
50. S. Backus, M. Kirchner, C. Durfee, M. Murnane, and H. Kapteyn, "Direct diode-pumped Kerr lens 13 fs Ti:sapphire ultrafast oscillator using a single blue laser diode," Opt. Express **25**, 12469–12477 (2017).
51. A. M. Kowalevicz, A. Sennaroglu, A. T. Zare, and J. G. Fujimoto, "Design principles of Q-preserving multipass-cavity femtosecond lasers," J. Opt. Soc. Am. B **23**, 760–770 (2006).
52. A. Dubietis and A. Couairon, *Ultrafast Supercontinuum Generation in Transparent Solid-State Media* (Springer, 2019).
53. F. Gravier and B. Boulanger, "Cubic parametric frequency generation in rutile single crystal," Opt. Express **14**, 11715–11720 (2006).
54. A. Borne, P. Segonds, B. Boulanger, C. Félix, and J. Debray, "Refractive indices, phase-matching directions and third order nonlinear coefficients of rutile TiO_2 from third harmonic generation," Opt. Mater. Express **2**, 1797–1802 (2012).
55. D. Hahner, P. Steinleitner, Y. Chen, K. F. Mak, and V. Pervak, "Second and third-order dispersion compensating mirror pairs for the spectral range from 1.2-3.2 μm," Opt. Express **30**, 38709–38716 (2022).
56. N. Karpowicz, "LightwaveExplorer," GitHub (2023), https://github.com/NickKarpowicz/LightwaveExplorer.
57. C.-H. Lu, Y.-J. Tsou, H.-Y. Chen, B.-H. Chen, Y.-C. Cheng, S.-D. Yang, M.-C. Chen, C.-C. Hsu, and A. H. Kung, "Generation of intense supercontinuum in condensed media," Optica **1**, 400–406 (2014).
58. N. Garejev, G. Tamošauskas, and A. Dubietis, "Comparative study of multioctave supercontinuum generation in fused silica, YAG, and LiF in the range of anomalous group velocity dispersion," J. Opt. Soc. Am. B **34**, 88–94 (2017).
59. H. Liang, P. Krogen, R. Grynko, O. Novak, C.-L. Chang, G. J. Stein, D. Weerawarne, B. Shim, F. X. Kärtner, and K.-H. Hong, "Three-octave-spanning supercontinuum generation and sub-two-cycle self-compression of mid-infrared filaments in dielectrics," Opt. Lett. **40**, 1069–1072 (2015).
60. E. A. Stepanov, A. A. Lanin, A. A. Voronin, A. B. Fedotov, and A. M. Zheltikov, "Solid-state source of subcycle pulses in the midinfrared," Phys. Rev. Lett. **117**, 043901 (2016).
61. A. Dubietis, G. Tamošauskas, R. Šuminas, V. Jukna, and A. Couairon, "Ultrafast supercontinuum generation in bulk condensed media," Lith. J. Phys. **57**, 113–157 (2017).
62. R. Budriūnas, D. Kučinskas, and A. Varanavičius, "High-energy continuum generation in an array of thin plates pumped by tunable femtosecond IR pulses," Appl. Phys. B **123**, 212 (2017).
63. Y. Yang, W. Bi, X. Li, M. Liao, W. Gao, Y. Ohishi, Y. Fang, and Y. Li, "Ultrabroadband supercontinuum generation through filamentation in a lead fluoride crystal," J. Opt. Soc. Am. B **36**, A1–A7 (2019).
64. S. Friberg and P. Smith, "Nonlinear optical glasses for ultrafast optical switches," IEEE J. Quantum Electron. **23**, 2089–2094 (1987).
65. M. E. Lines, "Influence of d orbitals on the nonlinear optical response of transparent transition-metal oxides," Phys. Rev. B **43**, 11978–11990 (1991).
66. F. A. Grant, "Properties of rutile (titanium dioxide)," Rev. Mod. Phys. **31**, 646–674 (1959).
67. W. Kang and M. S. Hybertsen, "Quasiparticle and optical properties of rutile and anatase TiO_2," Phys. Rev. B **82**, 085203 (2010).
68. A. Marcinkevičiūtė, G. Tamošauskas, and A. Dubietis, "Supercontinuum generation in mixed thallous halides KRS-5 and KRS-6," Opt. Mater. **78**, 339–344 (2018).
69. P. He, Y. Liu, K. Zhao, H. Teng, X. He, P. Huang, H. Huang, S. Zhong, Y. Jiang, S. Fang, X. Hou, and Z. Wei, "High-efficiency supercontinuum generation in solid thin plates at 0.1 TW level," Opt. Lett. **42**, 474–477 (2017).
70. J. Qian, Y. Peng, Y. Li, B. Shao, Z. Liu, W. Li, R. Feng, L. Shen, Y. Leng, and R. Li, "Few-cycle mid-infrared laser based on nonlinear self-compression in solid thin plates," Opt. Lett. **46**, 5075–5078 (2021).
71. R. Boyd, *Nonlinear Optics*, 3rd ed. (Academic, 2008).
72. Y. Deng, Y. L. Du, M. S. Zhang, J. H. Han, and Z. Yin, "Nonlinear optical properties in $SrTiO_3$ thin films by pulsed laser deposition," Solid State Commun. **135**, 221–225 (2005).
73. G. Marcaud, S. Serna, K. Panaghiotis, C. Alonso-Ramos, X. L. Roux, M. Berciano, T. Maroutian, G. Agnus, P. Aubert, A. Jollivet, A. Ruiz-Caridad, L. Largeau, N. Isac, E. Cassan, S. Matzen, N. Dubreuil, M. Rérat, P. Lecoeur, and L. Vivien, "Third-order nonlinear optical susceptibility of crystalline oxide yttria-stabilized zirconia," Photonics Res. **8**, 110–120 (2020).
74. T. D. Krauss and F. W. Wise, "Femtosecond measurement of nonlinear absorption and refraction in CdS, ZnSe, and ZnS," Appl. Phys. Lett. **65**, 1739–1741 (1994).
75. Y. Zheng, C. Sun, B. Xiong, L. Wang, Z. Hao, J. Wang, Y. Han, H. Li, J. Yu, and Y. Luo, "Integrated gallium nitride nonlinear photonics," Laser Photonics Rev. **16**, 2100071 (2022).
76. D. Milam, M. J. Weber, and A. J. Glass, "Nonlinear refractive index of fluoride crystals," Appl. Phys. Lett. **31**, 822–825 (1977).
77. G. N. Patwardhan, J. S. Ginsberg, C. Y. Chen, M. M. Jadidi, and A. L. Gaeta, "Nonlinear refractive index of solids in mid-infrared," Opt. Lett. **46**, 1824–1827 (2021).
78. J. Gu, A. Schweinsberg, L. Vanderhoef, M. Tripepi, A. Valenzuela, C. Wolfe, T. R. Ensley, E. Chowdhury, and M. Kolesik, "Random quasi-phase-matching in polycrystalline media and its effects on pulse coherence properties," Opt. Express **29**, 7479–7493 (2021).
79. M. N. Polyanskiy, "Refractive index database," https://refractiveindex.info.
80. J. W. Fleming, M. J. Weber, G. W. Day, *et al.*, *Handbook of Optical Materials* (CRC Press, 2018).
81. S. Okubo, A. Onae, K. Nakamura, T. Udem, and H. Inaba, "Offset-free optical frequency comb self-referencing with an f-2f interferometer," Optica **5**, 188–192 (2018).
82. B. Borchers, A. Anderson, and G. Steinmeyer, "On the role of shot noise in carrier-envelope phase stabilization," Laser Photonics Rev. **8**, 303–315 (2014).
83. T. D. Shoji, W. Xie, K. L. Silverman, A. Feldman, T. Harvey, R. P. Mirin, and T. R. Schibli, "Ultra-low-noise monolithic mode-locked solid-state laser," Optica **3**, 995–998 (2016).
84. R. Liao, H. Tian, T. Feng, Y. Song, M. Hu, and G. Steinmeyer, "Active f-to-2f interferometer for record-low jitter carrier-envelope phase locking," Opt. Lett. **44**, 1060–1063 (2019).
85. J. M. Dudley, G. Genty, and S. Coen, "Supercontinuum generation in photonic crystal fiber," Rev. Mod. Phys. **78**, 1135–1184 (2006).

86. N. Raabe, T. Feng, T. Witting, A. Demircan, C. Brée, and G. Steinmeyer, "Role of intrapulse coherence in carrier-envelope phase stabilization," Phys. Rev. Lett. **119**, 123901 (2017).
87. I. T. Sorokina, E. Sorokin, S. Mirov, V. Federov, V. Badikov, V. Panyutin, A. D. Lieto, and M. Tonelli, "Continuous-wave tunable Cr^{2+}:ZnS laser," Appl. Phys. B **74**, 607–611 (2002).
88. Y. Wang, T. T. Fernandez, N. Coluccelli, A. Gambetta, P. Laporta, and G. Galzerano, "47-fs Kerr-lens mode-locked Cr:ZnSe laser with high spectral purity," Opt. Express **25**, 25193–25200 (2017).
89. X. Bu, D. Okazaki, and S. Ashihara, "Inherent intensity noise suppression in a mode-locked polycrystalline Cr:ZnS oscillator," Opt. Express **30**, 8517–8525 (2022).
90. T. Fuji, J. Rauschenberger, C. Gohle, A. Apolonski, T. Udem, V. S. Yakovlev, G. Tempea, T. W. Hänsch, and F. Krausz, "Attosecond control of optical waveforms," New J. Phys. **7**, 116 (2005).
91. W. P. Putnam, P. D. Keathley, J. A. Cox, A. Liehl, A. Leitenstorfer, and F. X. Kärtner, "Few-cycle, carrier–envelope-phase-stable laser pulses from a compact supercontinuum source," J. Opt. Soc. Am. B **36**, A93–A97 (2019).
92. I. Pupeza, C. Zhang, M. Högner, and J. Ye, "Extreme-ultraviolet frequency combs for precision metrology and attosecond science," Nat. Photonics **15**, 175–186 (2021).
93. I. Pupeza, M. Huber, M. Trubetskov, *et al.*, "Field-resolved infrared spectroscopy of biological systems," Nature **577**, 52–59 (2020).
94. C. Manzoni, O. D. Mücke, G. Cirmi, S. Fang, J. Moses, S.-W. Huang, K.-H. Hong, G. Cerullo, and F. X. Kärtner, "Coherent pulse synthesis: towards sub-cycle optical waveforms," Laser Photonics Rev. **9**, 129–171 (2015).